J Mater Sci (2009) 44:3438–3444
DOI 10.1007/s10853-009-3457-0

Particle size-dependent electrical properties of nanocrystalline NiO

Salah A. Makhlouf · Mohamed A. Kassem · M. A. Abdel-Rahim

Received: 14 January 2009 / Accepted: 1 April 2009 / Published online: 15 April 2009

Abstract Nickel oxide nanoparticles are formed by chemical precipitation and subsequent drying and calcinations at temperatures ≥523 K. Samples are characterized using X-ray diffraction and BET surface area measurements indicating the formation of a single NiO phase whose crystallite size increases with increasing calcination temperature. The electrical properties are examined by measuring DC and AC conductivities and dielectric properties as functions of temperature. Electrical conductivities first slightly increases with increasing particle size up to 7–10 nm and are about 8 orders of magnitude higher than that of NiO single crystals. Further increasing the particle size above 10 nm, leads to a monotonic decrease of conductivity. The data are discussed in view of variations of grain boundary as well as triple junction volume fractions as the particle size varies. At temperatures above $\theta_D/2$ (θ_D is the Debye temperature), the conductivity is ascribed to a band-like conduction due to the large polaron. The activation energy of conduction was found to be minimal for the highly conducting samples of 7–10 nm, and gradually increases to ~0.5 eV with increasing the particle size above 10 nm. For $T < \theta_D/2$, the conductivity is best described by variable–range–hopping models. Model parameters are thus estimated and presented as functions of particle size. Frequency as well as temperature dependencies of the AC conductivity and dielectric constant exhibit trends usually observed in carrier dominated dielectrics.

S. A. Makhlouf (✉) · M. A. Kassem · M. A. Abdel-Rahim
Department of Physics, Faculty of Science, Assiut University, Assiut 71516, Egypt
e-mail: smakhlouf@assiut.edu.eg; smakhlouf2@yahoo.com

Introduction

Fabrication and characterization of nanostructured materials has become the subject of intense research from both theoretical points of view as well as for their potential technological applications [1–6]. NiO was selected as a model system of the present study because of its interesting semiconducting properties and many technological applications such as its broad use as a p-type transparent conductor, a potentially useful material for memory devices, a functional sensor layer in chemical sensors, a conducting phase in the anodes of fuel elements, and as an antiferromagnetic layer in exchange biased read head devices [7–13].

Over the past decade, electrical, optical, and physiochemical properties of NiO thin films and nanoparticles have been extensively investigated [13–17]. It is well known that bulk NiO has a cubic (NaCl-type) structure with a lattice parameter of 0.4177 nm and is classified as a Mott–Hubbard insulator with very low conductivity of the order of 10^{-11} Ohm^{-1} m^{-1} at room temperature (RT) [18–25]. However, the conductivity is drastically increased when prepared in the form of thin films or consolidated nanoparticles [13, 16], due to the holes generated by Ni vacancies in the lattice. The electrical conduction is primarily ascribed to the hopping of holes associated with the Ni^{2+} vacancies. NiO nanoparticles and nanostructured thin films have been prepared by various processes, reactive sputtering [7, 8, 12], spray pyrolysis [14], sol–gel [15], chemical precipitation [16, 26–28], and electrical explosion of a Ni wire in oxygen atmosphere [29].

So far, and with few exceptions [14, 26], the conduction mechanism at low temperature has not been investigated. Moreover, the contribution of these hopping charge carriers to polarization is not fully understood [17]. In the present

article, we report on the electrical properties of NiO nanoparticles with emphasis on its dependence on particle size as well as the conduction mechanism in this system at low temperatures.

Experimental

Nickel hydroxide $Ni(OH)_2$ precursor was chemically precipitated by mixing a nickel nitrate $Ni(NO_3)_2{\cdot}6H_2O$ aqueous solution and an aqueous sodium hydroxide NaOH solution whose pH was $\sim$12 at RT. The resulting green gel was washed several times with double distilled water until free of sodium nitrate ions, centrifuged, and dried in air at 383 K. Samples of NiO were prepared by calcining portions of the dried gel in air for 3 h at various temperatures in the range 523 K $\leq T \leq$ 1,073 K. Eleven specimens are obtained and are given code names S_1, S_2,…S_{11}, respectively. A Nova 3200 BET surface area analyzer was used to measure the specific surface area of the particles via nitrogen gas adsorption. X-ray diffraction (XRD) patterns were obtained at RT using a Philips PW1700 diffractometer equipped with an automatic divergent slit. Diffraction patterns were obtained using CuK_α radiation ($\lambda = 0.15418$ nm) and a graphite monochromator. The resultant patterns were matched with standard data for NiO for the purpose of phase identification [30].

For electrical measurements, powder samples were pressed into pellets of thickness about 1 mm in a sample holder constructed from Teflon. DC electrical measurements were done using a Keithley 617 electrometer in the temperatures range 115–465 K. AC conductivity and dielectric constant were measured in the same temperature range using a Stanford research SR720 RLC meter in the C-D mode at four test frequencies. All measurements are done in vacuum of 10^{-3} Torr. A K-type thermocouple is used to measure the temperature using a Keithley 181 nanovoltmeter. All samples are preheated in vacuum to 500 K and cooled down to 115 K; the measurement is then done with increasing temperature at a rate of about 1 K/min.

Results and discussion

Structure and particle size

Figure 1 shows the XRD patterns of some representative samples. Analysis of the diffraction patterns reveals that the formed phase is pure fcc NiO without any observable traces of $Ni(OH)_2$ for samples annealed at temperatures $\geq$523 K. Full profile fitting including a base line of the diffraction patterns were done assuming pseudo Lorenzian

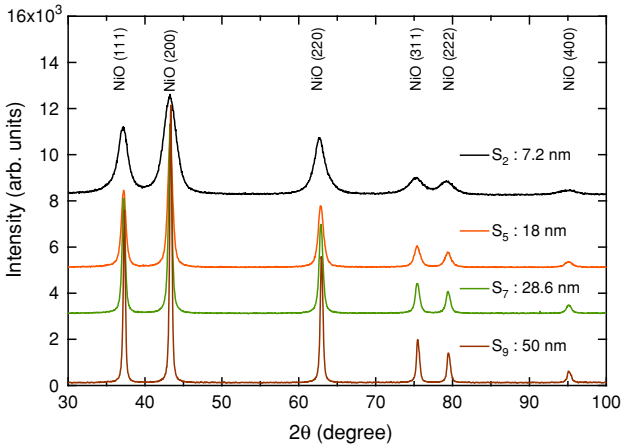

Fig. 1 XRD diffraction patterns of NiO nanoparticles

line shape, which accounts for the asymmetry for each peak, from which the Bragg angle, peak intensity, and the angular width at half maximum intensity (B) were determined. The particle size was estimated from XRD line broadening using a modified Debye Scherrer method [31]. In this method, plots of $(B - b)\cos\theta$ versus $2\sin\theta$ were extrapolated to zero to determine $(B - b)_0$, the value of peak broadening due to the crystallite size. Here θ is the Bragg angle and b is the instrumental broadening measured for a bulk polycrystalline NiO sample obtained from the same precursory after calcination at 1,273 K. The slope of the line is an indication of the fractional peak broadening arising from microstrains. The average particle size, d, was then calculated using $d = 0.9\lambda/(B - b)_0$, where λ is the wavelength of the radiation used. Particle size was moreover estimated from BET measurements assuming spherical shape of the particles and using density of bulk NiO for all samples. Figure 2 displays the variation of the particle size obtained by both methods with calcining temperature. Agreement between these two methods in estimating the particle size was excellent for average sizes $\leq$25 nm and rather satisfactory for larger sizes. In the following, we will

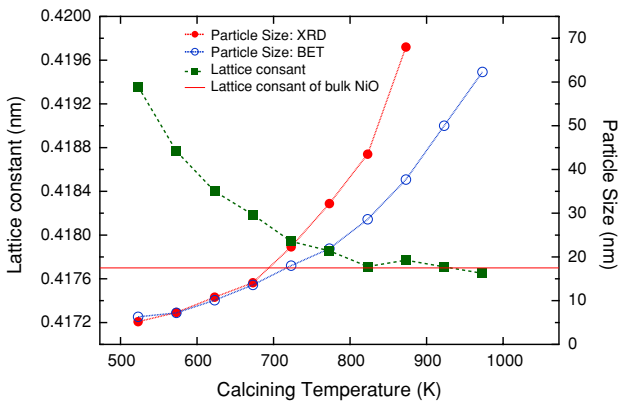

Fig. 2 Lattice constant and particle size of NiO nanoparticles as functions of calcining temperature

use the average particle size obtained from BET measurements.

Close inspection to the diffraction patterns of Fig. 1 indicates that the diffraction peaks showed a systematic shift to lower angles with decreasing particle size, which indicates lattice expansions at smaller particle sizes. The lattice constant was accurately determined using a least squares refinement program [32] and was found to increase above its bulk NiO value with decreasing particle size below 25 nm as shown in Fig. 2. The lattice expansion indicated in Fig. 2 corresponds to a negative pressure that was probably produced by the strong repulsive interactions of the parallel surface defect magnetic dipoles at small particle sizes. Similar nanoscale lattice modifications have been observed in same and other magnetic systems [26, 33]. The strongest peaks (200), (111), and (220) are used to calculate the texture grade of the samples and were found to be consistent with those of bulk NiO polycrystalline material [30], indicating perfect random crystalline orientations.

DC electrical conductivity

Size effect

Figure 3 displays the DC conductivity (σ) of the obtained pellets at different temperatures at and below RT as a function of particle size. It is important to note that the DC conductivities of all samples are much higher than that of NiO single crystals; for instance sample S_3 that has a 10 nm particle size exhibits a RT conductivity nearly 8 orders of magnitude higher than that of NiO single crystals at the same temperature [18]. Surface versus bulk conduction in pure stoichiometric NiO crystals has been discussed in details in ref. [34]. The main result was the existence of a less stoichiometric high conductivity surface layer of thickness about 50 atomic layers, which reveals a defect-dependent conductivity mechanism for the surface conduction [34]. Large conductivity of NiO nanoparticles are previously observed and ascribed to the presence of large number of Ni^{2+} vacancies [16] on the surface of the particle. Such vacancies correspond to an acceptor-like level in the energy gap close to the Fermi level just above the localized 3d band of Ni^{2+} and the wide 2p band of O^{2-} [16]. Presence of each Ni^{2+} vacancy in the lattice leads to the transformation of two adjacent Ni^{2+} ions into Ni^{3+} ions to acquire charge neutrality and induces a lattice distortion [19].

As shown in Fig. 3, the conductivity first increases with increasing particle size from 5 to 10 nm, whereas it decreases monotonically with increasing particle size above 10 nm. On the other hand, the RT conductivity of a sample with microsized particles obtained after calcinations at 1,473 K was found to be $\sim 10^{-9}$ Ohm^{-1} m^{-1}, only 2 orders of magnitude larger than that of NiO single crystals [18–25]. The result represents a finite-size phenomenon indicating various competing contributions to the conductivity as the particle size varies. A possible explanation of such dependence is to consider grain boundary as well as triple junction contributions to the conductivity, as a large portion of the material resides in the intercrystalline region [35–37]. Triple junctions are intersection lines of three or more adjoining crystallites and have a major contribution particularly for particle sizes less than 10 nm [36]. Neither spheres nor cubes are reasonable or suitable for driving triple junction volume fraction. Palumbo et al. [38] has previously considered the grains to have regular 14 sided tetrakaidecahedron shapes with hexagonal faces representing grain boundaries and edges corresponding to triple junctions. As shown in Fig. 4 and assuming the maximum diameter of an inscribed sphere as the grain size (d) and the intercrystalline component as an outer 'skin' of the tetrakaidecahedron with thickness of $\Delta/2$, the intercrystalline volume fraction has been calculated as:

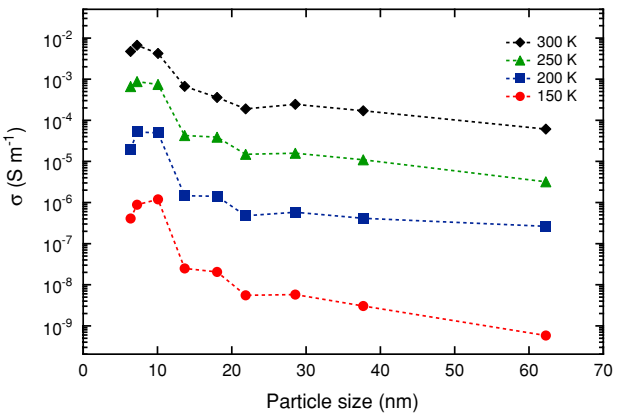

Fig. 3 DC conductivity as a function of particle size at indicated temperatures

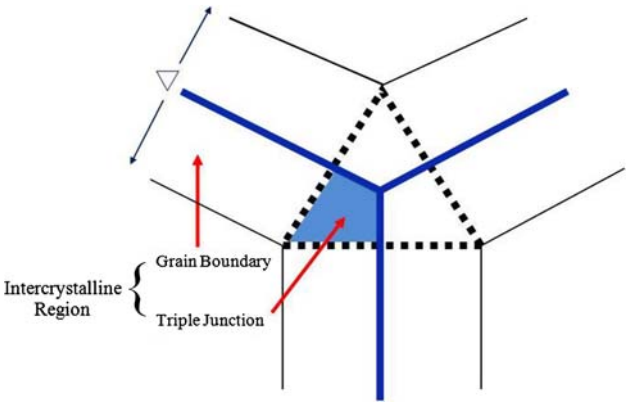

Fig. 4 Cross-sectional view of the intersection of three adjoining tetrakaidecahedra (along a polyhedral edge), where the triple junction is considered a triangular prism extending into the page [38]

$$V_{ic} = 1 - [(d - \Delta)/d]^3.$$

The grain boundary component has been assessed as:

$$V_{gb} = 1 - [3\Delta(d - \Delta)^2]/d^3$$

and, therefore, the volume fraction associated with triple junctions V_{tj} is then given by

$$V_{tj} = V_{ic} - V_{gb}.$$

All of the above equations are valid and have a physical sense for $d > 2\Delta$. Figure 5 displays the variation of V_{ic}, V_{gb}, and V_{tj} for $\Delta/2 = 0.5$ nm as functions of grain size (d) and suggests that these values can be as much as 70–80% at very small sizes 2–3 nm. V_{gb} slightly increases and then falls smoothly as the particle size increases, whereas V_{tj} falls sharply as the particle size increases from 2 to 10 nm. For nanoparticles with small average particle size, the effect of the intercrystal region in conductivity should be viewed as the sum of the contributions due to grain boundaries and triple junctions. It has been reported that in polycrystalline NiO samples, the grain boundary enhances the conductivity since it contains a large number of Ni^{2+} vacancies [18, 19, 39]. If we assume that the triple junctions have a reverse effect on conductivity, we obtain an effective volume fraction $V_{eff} = V_{gb} - V_{tj}$. The physical basis for this assumption lies in the fact that triple junctions, like dislocations, should correspond to maxima of a potential barrier, causing scattering of charge carriers and there by decreasing the electrical conductivity [37]. Assuming that the effects of grain boundary and triple junctions on conductivity are linear, we may account for the variation of the conductivity with grain size according to:

$$\sigma \propto V_{eff} = (V_{gb} - V_{tj}).$$

The variation of V_{eff} with particle size is shown in Fig. 5. This pattern is identical to the pattern of Fig. 3 and explains the observed variation of σ with particle size. It should also be mentioned that grain boundaries in NiO bi-crystals may increase or decrease the electrical conductivity by 2 orders of magnitude depending on the nature of the boundary, temperature, and pressure conditions [40].

Conduction mechanism

Figure 6 shows the temperature dependence of the conductivity of three samples (S_1, S_7, and S_{11}) of particle sizes 6.3, 28.6, and 100 nm presented in $\log(\sigma T)$ versus $1000/T$ plot. For sample with the largest particle size, the conductivity displays a plateau of slight slope at $T < 150$ K and increases rather linearly with increasing T for $T > 150$ K. Similar results are obtained for other samples whose particle sizes are greater than 25 nm. However, the temperature at which the linear curves bends to plateau shifts to lower temperatures with decreasing the particle size. For samples whose particle size are <25 nm, the temperature dependence of the conductivity is rather different; the plateau region does not exist in the studied temperature range down to 115 K.

In bulk NiO, at temperatures below 1,000 K, two competing mechanisms contribute to the conductivity, one due to small polarons in the 3d band of Ni^{2+} and the other due to large polarons in the 2p band of O^{2-} [19]. At temperatures above 100 K, small polarons conduct only by means of thermally activated hopping with activation energy of 0.01 eV [18, 25, 39]. On the other hand, in the temperature range 200–1,000 K, the band like conduction due to the large polarons in the 2p band of O^{2-} with activation energy of ~0.6 eV is dominating [19]. The result indicate that for samples with particle size larger than 25 nm, thermal activation hopping of small polarons is responsible for conductivity for temperatures below

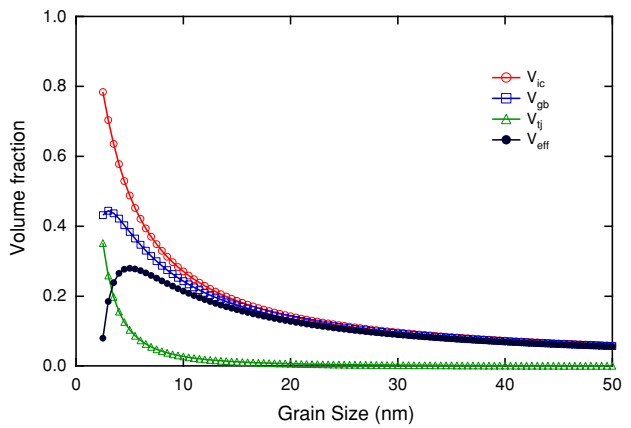

Fig. 5 Variation of volume fractions of total intercrystal (V_{ic}), grain boundaries (V_{gb}), triple junctions (V_{tj}), and effective (V_{eff}) regions as functions of average particle size

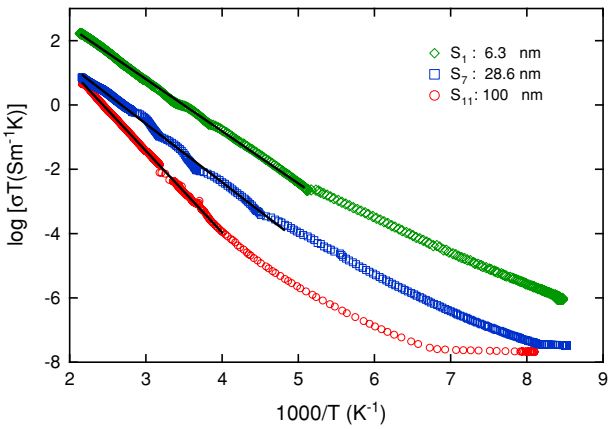

Fig. 6 Temperature variation of the DC conductivity of NiO nanoparticles at indicated particle size. *Solid lines* are the linear fits for $T > \theta_D/2$

150 K. While above 150 K, the conductivity curves become rather linear, at higher temperatures deviation from linear behavior occurs around $\theta_D/2$ (200–250 K, depending on the particle size), where θ_D is the Debye temperature. The activation energy for conduction (ΔE) was estimated from such high temperature linear fits shown in Fig. 6, using the equation $\sigma = (\sigma_0/T)\exp(-\frac{\Delta E}{k_B T})$. ΔE shows a minimum of about 0.30 eV for the 7–10 nm size particles and increases with further increasing the particle size and becomes 0.5 eV for the largest ones as displayed in Table 1. Similar particle size dependence of ΔE has been previously observed for grain as well as grain boundary conduction in the same system [26]. In Table 1, θ_D is quoted within an error at most ±10 K due to the uncertainty of determining the exact temperature at which the curves deviates from linearity.

At low temperatures ($T < \theta_D/2$), the temperature dependence of the conductivity presented in Fig. 6 is deviated from linearity, the data are thus represented in a different formalism. We attempted to apply the variable–range–hopping (VRH) models proposed by Mott [41, 42] and Greaves [43]. In Mott model, the conduction is based on a single optical phonon approach and the conductivity is expressed as:

$$\sigma = A\exp\left(-\frac{T_0}{T}\right)^{1/4}$$

where

$$T_0 = 256[2\alpha^3/9\pi k_B N(E_F)]$$

and

$$A = [e^2/2(8\pi)^{1/2}]v_o[N(E_F)/\alpha k_B T]^{1/2}.$$

$N(E_F)$ is the density of states at the Fermi level A and T_0 are obtained from the log(σ) versus $T^{-1/4}$ plots shown in Fig. 7. It is commonly held that much use of the exponent T_0 has been made to extract values of $N(E_F)$, given assuming values for $\alpha = 10\ \text{nm}^{-1}$ [44, 45]. The values of the exponent T_0 and $N(E_F)$ are displayed in Table 1 as functions of particle size. T_0 was found close to those reported in various transition metal oxide glasses [45]. We further apply Greaves formula [43] for the VRH, which is known to be valid for the intermediate range of temperature below $\theta_D/2$. In view of this model, the conductivity is given as:

$$\sigma T^{1/2} = B\exp\left(-\frac{T_0}{T}\right)^{1/4}, \quad T_0 = (2.1)^4[\alpha^3/k_B N(E_F)].$$

Figure 8 displays the log($\sigma T^{1/2}$) versus $T^{-1/4}$ plots for some representative samples. The data are typically linear confirming Greaves model. The fitting parameters obtained for this model are also displayed in Table 1. It is obvious that the two VRH models are found suitable to explain the low temperature conductivity data below $\theta_D/2$.

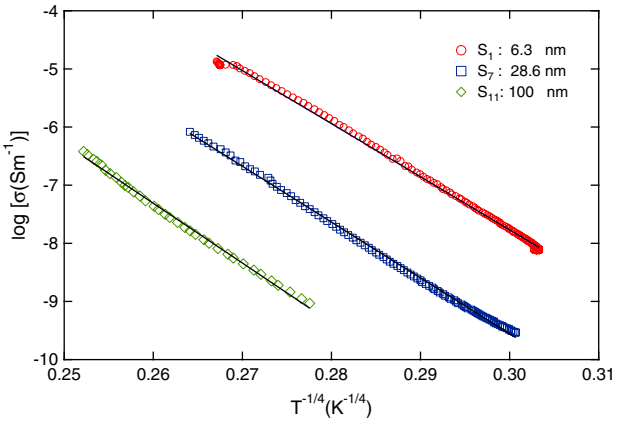

Fig. 7 Dependence of log(σ) on $T^{-1/4}$ of NiO nanoparticles. The *solid lines* are the linear fits for $T < \theta_D/2$

Table 1 Electrical parameters of NiO nanoparticles as functions of particle size

Code	Calcining temperature (K)	d_{BET} (nm)	ΔE (eV)	θ_D (±10 K)	Mott model parameters		Greaves model parameters	
					T_0 (K)	$N(E_F)$ ($\times 10^{19}$ eV^{-1} cm^{-3})	T_0 (K)	$N(E_F)$ ($\times 10^{19}$ eV^{-1} cm^{-3})
S_1	523	6.30	0.32	392	19.52×10^8	10.75	22.25×10^8	10.13
S_2	573	7.20	0.29	388	22.88×10^8	9.17	25.98×10^8	8.68
S_3	623	10.1	0.30	392	17.37×10^8	12.08	19.88×10^8	11.34
S_4	673	13.6	0.34	400	19.13×10^8	10.96	21.86×10^8	10.32
S_5	723	18.0	0.34	404	25.74×10^8	8.15	29.19×10^8	7.72
S_6	773	21.9	0.32	422	30.00×10^8	6.99	33.86×10^8	6.66
S_7	823	28.6	0.36	414	23.91×10^8	8.77	27.11×10^8	8.32
S_8	873	37.7	0.38	462	29.39×10^8	7.14	33.24×10^8	6.78
S_9	923	50.0	0.43	482	32.72×10^8	6.41	36.98×10^8	6.10
S_{10}	973	62.3	0.44	486	26.64×10^8	7.88	30.33×10^8	7.43
S_{11}	1,073	100	0.50	500	31.27×10^8	6.71	35.48×10^8	6.36

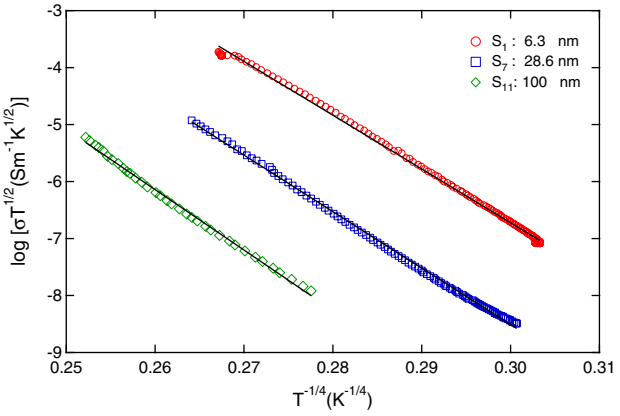

Fig. 8 Dependence of $\log(\sigma T^{1/2})$ on $T^{-1/4}$ of NiO nanoparticles. The *solid lines* are the linear fits for $T < \theta_D/2$

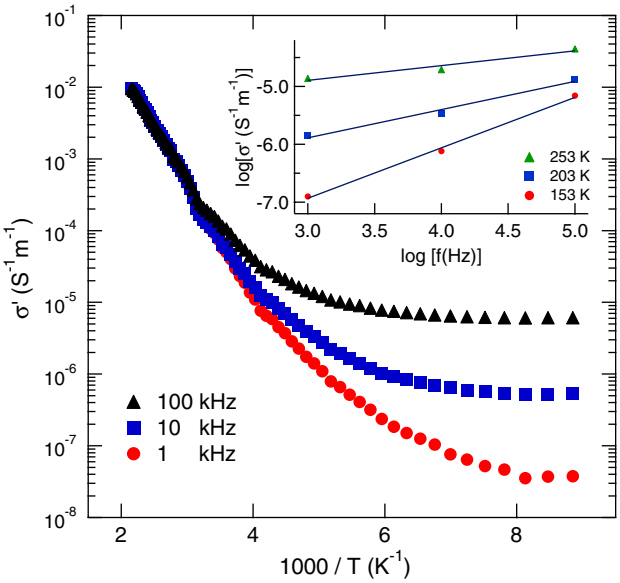

Fig. 9 AC conductivity of S_5 (18 nm) measured at three test frequencies as a function of temperature. Inset is a log–log plot for estimating the exponent n at indicated temperatures

AC electrical properties

Figure 9 displays the variation of the AC conductivity with temperature for sample S_5 (18 nm) at indicated frequencies. The conductivity increases with increasing temperature at all frequencies implying that more charge carriers are produced at higher temperatures, contributing to the AC conductivity. It is clear that the conductivity is higher at higher frequencies confirming polaron hopping at low temperatures in the present system [46]. As shown in the inset of Fig. 9, the σ' increases with increasing f and is a power function of f with an exponent $n = 0.87$ at 153 K, which is very close to the previously reported values in NiO films and nanoparticles [28, 29]. Similar trends are observed for other samples with different particle sizes.

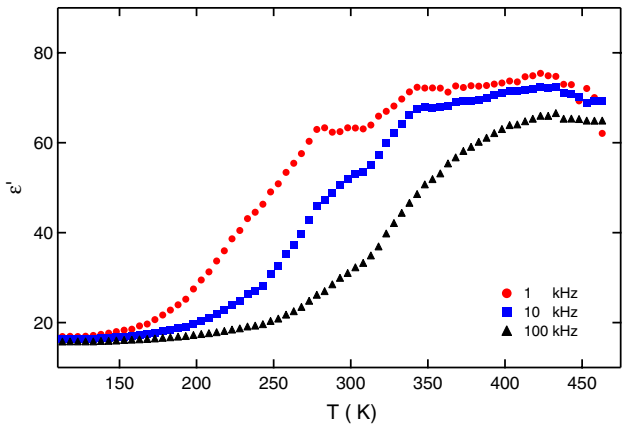

Fig. 10 Dielectric constant of S_5 (18 nm) measured at three test frequencies as a function of temperature

Figure 10 displays the variation of the real part of the dielectric constant, ε', with temperature of S_5 (18 nm) at indicated test frequencies. It can be seen that ε' in the range 1–100 kHz decreases with increasing frequency at constant temperature. On the other hand, ε' increases with increasing temperature at constant frequency. The higher dielectric constant at higher temperatures can be understood in view of the increase of the concentration of charge carriers with increasing temperature as usually observed in carrier dominated dielectrics. The increase of the ε' with increasing temperature over the three test frequencies for all the samples with well-defined activation energies means that the polarization is due to some thermally activated mechanisms such as charge carrier transport rather than due to permanent dipoles [47]. It should be mentioned that details of the dielectric behavior and AC conductivity as functions of particle size in a wider frequency range for the present system is under study.

Conclusion

Nickel oxide nanoparticles whose crystallite size varies from 6 to 100 nm are obtained by a chemical route. Particle size as well as temperature dependencies of the electrical properties are studied. Electrical conductivities first slightly increases with increasing particle size up to ~10 nm and are about 8 orders of magnitude higher than that of NiO single crystals and decreases with further increase of the particle size. For $T > \theta_D/2$, the conductivity is ascribed to a band like conduction due to the large polaron. The activation energies showed a minimum of about 0.3 eV corresponding to 6–10 nm size particles, and increases monotonically to ~0.5 eV for the largest particles. For $T < \theta_D/2$, the conductivity is best described by VRH models. Frequency as well as temperature dependencies of

the AC conductivity and dielectric constant exhibit trends usually observed in carrier dominated dielectrics.

Acknowledgement The authors are indebted to Dr. H. Alattar for his discussion and Prof. A. A. Bahgat (Al-Azhar University) for critical reading of the manuscript.

References

1. Gleiter H (1989) Prog Mater Sci 33:223
2. Siegel RW (1990) MRS Bull 15:60
3. Siegel RW (1991) Annu Rev Mater Sci 21:559
4. Siegel RW (1991) In: Chan RW (ed) Materials science and technology, vol 15. Processing of metals and alloys. VCH, Wienheim
5. Gleiter H (1992) Nanostruct Mater 1:1
6. Siegel RW (1994) In: Fujita FE (ed) Physics of new materials. Springer, Berlin
7. Hotovy I, Buc D, Hascik S, Nennewitz O (1998) Vacuum 50:41
8. Hotovy I, Huran J, Spiess L, Liday J, Sitter H, Hascik S (2003) Vacuum 69:237
9. Fujii E, Tomozawa A, Torii H, Takayama R (1996) Jpn J Appl Phys 35:L328
10. Estrada W, Andersson A, Granqvist C (1998) J Appl Phys 64:3678
11. Azens A, Kullman L, Vaivars G, Nordborg H, Granqvist C (1998) Solid State Ion 113:449
12. Lee JW, Park IH, Chung CW (2005) Integr Ferroelectr 74:71
13. Makhlouf SA (2008) Thin Solid Films 516:3112
14. Patil PS, Kadam LD (2002) Appl Surf Sci 199:211
15. Boscloo G, Hagfeldt A (2001) J Phys Chem B 105:3039
16. Biju V, Abdul Khadar M (2001) Mater Res Bull 36:21
17. Biju V, Abdul Khadar M (2003) J Mater Sci 38:4055. doi:10.1023/A:1026131103898
18. Morin FJ (1954) Phys Rev B 93:1199
19. Adler D, Feinleib J (1970) Phys Rev B 2:3112
20. Bosman AJ, Vandaal HJ (1970) Adv Phys 19:1
21. Pushparajah P, Radhakrishna S (1997) J Mater Sci 32:3001. doi:10.1023/A:1018657424566
22. Bosman AJ, Crevecoeur C (1965) Phys Rev 144:763
23. Van Houten S (1960) J Phys Chem Solids 17:7
24. Heikes RR, Johnston WD (1957) J Chem Phys 26:582
25. Lunkenheimer P, Loidl A, Ottermann CR, Bange K (1991) Phys Rev B 44:5927
26. Li L, Chen L, Qihe R, Li G (2006) Appl Phys Lett 89:134102
27. Richardson JT, Yiagas DI, Turk B, Forster K (1991) J Appl Phys 70:6977
28. Makhlouf SA, Parker FT, Spada FE, Berkowitz AE (1997) J Appl Phys 81:5561
29. Kotov YA, Bagazeyev AV, Beketov IV, Murzakaev AM, Samatov OM, Medvedev AI, Moskalenko NI, Timoshenkova OR, Demina TM, Shtolts AK (2005) Tech Phys 50:1279. Translated from Zhurnal TekhnicheskoïFiziki (2005) 75:29
30. Powder Diffraction File JCPDS-International Centre for Diffraction Data (1999) ICDD Card No. 47-1049
31. Williamson GK, Hall WH (1953) Acta Metall 1:22
32. Holland TJB, Redfern SAT (1997) Miner Mag 61:65
33. Nunes AC, Yang L (1998) Surf Sci 399:225
34. Wittenauer MA, Van Zandt LL (1982) Philos Mag B 46:659
35. Suryanarayan C (1994) Bull Mater Sci 17:307
36. Bollman W (1984) Philos Mag A 49:73
37. Meilikhov EZ, Farzetdinova RM (1998) Physica E 3:190
38. Palumbo G, Thorpe SJ, Aust KT (1990) Scr Metall Mater 24:1347
39. Snowden DP, Saltzburg H (1965) Phys Rev Lett 14:497
40. Osburn CM, Vest RW (1971) J Phys Chem Solids 32:1355
41. Mott NF (1968) J Non-Cryst Solids 1:1
42. Mott NF (1969) Philo Mag 19:835
43. Greaves GN (1973) J Non-Cryst Solids 11:427
44. Elliot SR (1984) Physics of amorphous materials. Longman, London and New York
45. El-Desoky MM (2003) J Mater Sci Mater Electron 14:215
46. Austin I, Mott NF (1969) Adv Phys 18:41
47. Jonscher AK, Reau JM (1978) J Mater Sci 13:563. doi:10.1007/BF00541806